INL/JOU-20-59496-Revision-0

Feasibility Assessment of a Natural-Circulation Salt Irradiation Loop in the Advanced Test Reactor

March 2021

Abdalla Abou Jaoude, Samuel Walker, Sandesh Bhaskar, Wei Ji

Changing the World's Energy Future

INL is a U.S. Department of Energy National Laboratory operated by Battelle Energy Alliance, LLC

INL/JOU-20-59496-Revision-0

Feasibility Assessment of a Natural-Circulation Salt Irradiation Loop in the Advanced Test Reactor

Abdalla Abou Jaoude, Samuel Walker, Sandesh Bhaskar, Wei Ji

March 2021

Idaho National Laboratory
Idaho Falls, Idaho 83415

http://www.inl.gov

Prepared for the
U.S. Department of Energy
Under DOE Idaho Operations Office
Contract DE-AC07-05ID14517

Feasibility Assessment of a Natural-Circulation Salt Irradiation Loop in the Advanced Test Reactor

Abdalla Abou-Jaoude[a]*, Samuel A. Walker[b], Sandesh Bhaskar[c], and Wei Ji[b]

[a]*Idaho National Laboratory, Nuclear Science & Technology, Idaho Falls, Idaho*

[b]*Rensselear Polytechnic Institute, Nuclear Engineering Program, Troy, New York*

[c]*North Carolina State University, Nuclear Engineering, Raleigh, North Carolina*

*Email: abdalla.aboujaoude@inl.gov

Feasibility Assessment of a Natural-Circulation Salt Irradiation Loop in the Advanced Test Reactor

Molten-salt reactors (MSRs) will likely require some level of irradiation testing as part of their licensing basis. An ideal experiment would consider the integrated effect of neutron flux and fission product generation in addition to circulating flow conditions. The feasibility of a natural-circulation irradiation salt loop in the Advanced Test Reactor (ATR) is assessed here. The flow is induced by the innovative combination of gas-gaps and fin-gaps along the capsule wall to fine-tune radial heat conductance and therefore drive an axial temperature gradient across the experiment height. Following multiple design optimizations, a promising configuration was identified. The 45-kW experiment would generate a 0.15 m/s flow velocity with 6 kg of fuel-bearing salt. This demonstrates the possibility of generating appreciable flow rates within manageable experimental conditions (e.g., total size and heat generation). An initial assessment of species mass tracking inside the experiment was also performed to gain an understanding of radionuclide behavior within the system. Results showed that significant quantities of Xe can be extracted in the off-gas (1.7 kCi) for 8% bubble removal efficiency rate. These results highlight the potential value of such experiments. Further work will involve detailed engineering drawings and analyses of the loop, as well as more computationally expensive modeling of species mass tracking.

Keywords: molten salt, irradiation loop, neutron transport, thermal hydraulics, species tracking

I. INTRODUCTION

I.A. The Need for Salt Irradiation Experiments

Interest in molten-salt reactors (MSRs) has substantially increased during the past decade. Many companies are developing a wide range of concepts, many of which propose to use novel salts that have limited or no irradiation data. Such testing will likely be necessary for the licensing basis of these novel concepts. Three key types of phenomena inside the reactor will heavily impact the salt behavior: (1) gamma-based (primarily through salt radiolysis), (2) neutron-induced (namely, the transmutation of

the solvent elements), and (3) fission-based (the high kinetic energy of fission fragments can impact the salt molecules). All these will strongly affect important reactor characteristics: the evolution of salt thermophysical properties, distribution of radionuclides (dissolved, volatile, or plating), and corrosion of the salt-wall boundary.

Source-term release from a molten salt depends on a range of phenomena difficult to reproduce out-of-pile: solubility limits, gaseous species transport, radiolysis, and thermodynamics are all interdependent and are affected by the radiation environment. Recent studies used thermodynamic models in an attempt to quantify how some of the more problematic isotopes (Cs and I) are released during hypothetical temperature excursion that raises a given fluoride salt temperature from 350 to 1500 K [1]. In addition to thermodynamic volatilization, recent studies have shown that long-lived transient radical species form in molten salts as a result of ionizing radiation. More specifically, monatomic chlorine/fluorine radicals and solvated electrons were both observed during pulsed radiolysis experiments [2]–[6]. Of particular concern is radiolysis of the salt due to the recombination of two radicals to form gaseous Cl_2 or F_2. The irradiation dose (and resulting radicals) can also impact the formation of volatile radionuclide species, due to the increase in the concentration of precursor radical species. This dynamic is mainly driven by the salt recombination kinetics, dose rate, and radiation type (i.e., gamma, neutron, ionized fission fragments, etc.).

Additionally, predicting the behavior of materials exposed to MSR conditions is challenging due to the simultaneous presence of high temperatures and radiation dose rates, in addition to the continual evolution of salt chemistry over time. For instance, during the Molten Salt Reactor Experiment (MSRE) operations, tellurium was unexpectedly found to cause accelerated degradation of the vessel through reactions with specific alloying elements, resulting in intergranular corrosion and cracking [7].

Although some similarity in the corrosion mechanisms of chloride and fluoride salts have been observed, the impact of many species (e.g., tellurium) is relatively unknown in chlorides [8]. A salt irradiation loop could elucidate the combined effect of fission products, radiolysis-induced radical species, and radiation damage on material corrosion. None of these three effects can be adequately replicated out-of-pile.

Long-term operation of an MSR results in the accumulation of soluble fission products, leading to dynamic changes in salt chemistry that subsequently affect thermophysical properties. The extent to which irradiation and fission product buildup affect chloride salt properties is currently unknown. While some studies advocate using non-radioactive fission products (surrogates) to measure this effect [9], these approaches must still be qualified using irradiation data. Furthermore, for reasons already stated, it is difficult to predict the exact proportion of soluble and semi-soluble species in the salt. This hinders the ability to simulate irradiated salt out-of-pile using surrogates. Consequently, post-irradiation data collected on salt properties are of great importance for a future licensing basis for reactors.

Because of these various effects, irradiation experiments are expected to provide invaluable data to MSR vendors. To this end, an integral effects test that can account for the impacts of temperature gradients, velocity profiles, and irradiation would be ideal.

I.B. Background on VESIL

To provide the capability for an integrated effects testing platform to study the mechanisms outlined above for MSRs, the Versatile Experimental Salt Irradiation Loop (VESIL) is currently under consideration at Idaho National Laboratory (INL) for deployment in the Advanced Test Reactor (ATR) [10]. A feasibility assessment of this capability is carried out in this research article. The main intent is to demonstrate that

this type of integral effects test can provide useful information to MSR designers such as mass flow rates, temperature profiles and fission rates. A schematic illustration of the loop is shown in Figure 1. Natural circulation was opted for, following an INL internal review that concluded that the development needs for a pump capable of withstanding the high neutron flux in the ATR and the corrosive salt environment would be prohibitive [10].

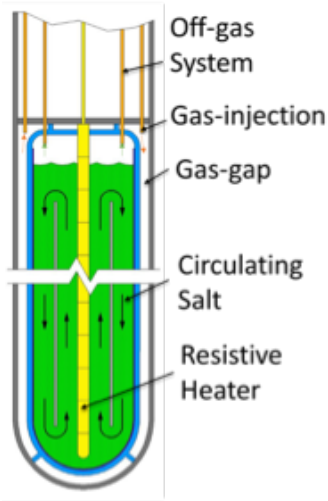

Figure 1. Illustration of the VESIL concept. The temperature gradients induce natural circulation of the molten salt. Two wall boundaries provide additional barriers to release. Taken from [10].

The ATR is considered a promising host reactor for VESIL, in light of its high flux and long track record of testing complex experiments. Table I summarizes some of the ATR's operating specifications. The length of each operating cycle has slowly increased over the years, from 40 to 50 days in the early 2000's to an average of 60 days over the last several years (the duration selected for this analysis).

Table I. ATR operation parameters used in the analysis. Based on [11].

Parameter	Value
Power	110 MW_{th}
Irradiation days	60
Number of flux traps	9

Number of experiment positions	68
Number of fuel assemblies	40
Active length of assemblies	121.92 cm
Operating pressure	2.7 MPa
Coolant T_{in}/T_{out}	52/71°C

1

2 The ATR can simultaneously host a range of experiments, as highlighted in
3 Figure 2. The so-called A-, B-, and H-positions see the highest fluxes but are usually
4 highly sought-after and have more stringent safety requirements. O-positions see
5 significantly reduced fluxes but may be of interest if other options are unavailable. It
6 was concluded that the I-positions struck the right balance of attractive features:
7 relatively high flux, larger experimental volume, medium demand from other
8 customers, and reduced safety concerns (due to their relative distance from the fuel).

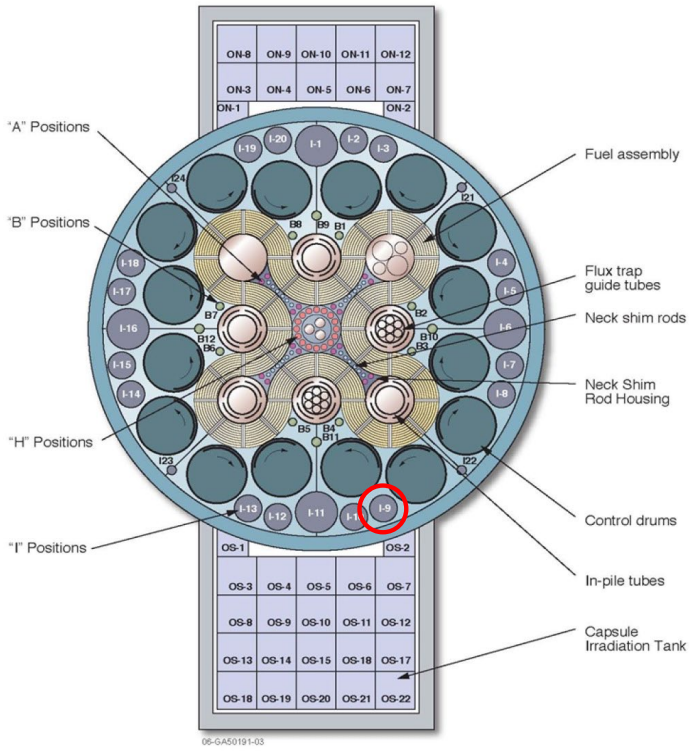

Figure 2. Diagram of the ATR, highlighting the main I-position considered for this analysis. Taken from [11].

Although the ATR has never hosted a salt-based irradiation, a breadth of historical experiments performed in other reactors can be leveraged in designing such a capability. Table II summarizes the most relevant example cases. It is interesting to observe the relative complexity of older experiments compared to more recent ones that tend to be static and non-fueled. The experiences in two previous research reactors, MTR (the predecessor to ATR) [12] and ORR [13], are particularly insightful. The ORR loop relies on natural circulation, as is the case with VESIL; however, it is rather bulky and placed in the reactor beam-port. Meanwhile, the MTR experiment is compact (cartridge-type) and positioned closer to the core but relies on a small pump to circulate the salt. In essence, VESIL would combine both of these concepts. More recently, MIT demonstrated the ability to handle off-gas from a salt (in this case, tritium) [14], and the HFR (research reactor in Petten, Netherlands) demonstrated the ability to irradiate (fertile) fuel-bearing salt [15].

Table II. Historical overview of relevant in-pile salt experiments.

Reactor	Salt Type	Structure	Year	T_{max}	Circulation	Ref.
LITR	$NaF\text{-}ZrF_4\text{-}UF_4$	Inconel	1956	870°C	forced	[16]
MTR	$NaF\text{-}ZrF_4\text{-}UF_4$	Inconel + Hastelloy N	1958	870°C	forced	[12]
ORR	$LiF\text{-}BeF_2\text{-}ZrF_4\text{-}UF_4$	Hastelloy N	1966	650°C	natural	[13]
LR-0	$LiF\text{-}BeF_2$	Graphite	2017	700°C	static	[17]
MITR	$LiF\text{-}BeF_2$	Graphite	2017	700°C	static	[14]
OSURR	KCl-MgCl	Mo alloy	2018	800°C	static	[18]
HFR	$LiF\text{-}ThF_4$	Graphite	2018	600°C	static	[15]

The analysis here focuses on demonstrating that, from an experimental standpoint, a natural-circulation salt loop driven by fission energy can reach appreciable velocities and generate useful amounts of radionuclides. The analysis is divided into three main sections. A neutron transport code is used to evaluate loop performance and estimate the power distribution, then a thermal-hydraulics code uses this data to determine the natural-circulation velocity in a given loop design. Lastly, a code with species mass tracking capabilities is used to estimate the generation rate and mass transport of certain radionuclides of interest. The steps outlined below will be discussed in greater detail in Section II.

1. Neutron transport simulations
    a. Explicitly model the experiment in the ATR.
    b. Specify the experiment dimensions and the insertion depth into the core.
    c. Obtain the power distribution inside the loop.
2. Thermal-hydraulic simulations
    a. Evaluate the natural circulation flow using 1-D channel analysis.

b. Select thermal conductivities to the ATR coolant heat sink.

c. Obtain the temperature distribution and flow field inside the loop.

3. Isotope generation and species mass transport

a. Track isotope generation and decay chains.

b. Account for the bubbling of fission products out of the salt, and the plating onto walls.

II. DESIGN EVALUATION APPROACH

II.A. Neutron Transport Model

Neutron transport code MCNP6 (Monte Carlo Neutral Particle) was selected for this analysis [19]. It is a generalized-geometry, continuous-energy, Monte Carlo, neutron transport code capable of modeling the ATR's complex geometries and accounting for all relevant details. More specifically, the MCNP6 model developed for the ATR 94cic benchmark (a well characterized core layout from 1994) was used [1]. A total of 1.88×10^8 particle histories (3,750 cycles, of which 250 were inactive) was deemed sufficient to analyze the experiment positions considered in this work. The resulting Monte Carlo standard deviation on the eigenvalue was 6 pcm. Both the neutron and gamma particles were tracked to accurately account for heat generation within VESIL.

As shown in Figure 3, the VESIL experiment is explicitly modeled inside the ATR position to account for spatial self-shielding effects. Following a review by experiment safety analysts, the I-positions were concluded to be the most desirable for an initial salt-bearing experiment in the ATR. As a result, the current work focuses on the medium and large I-positions.

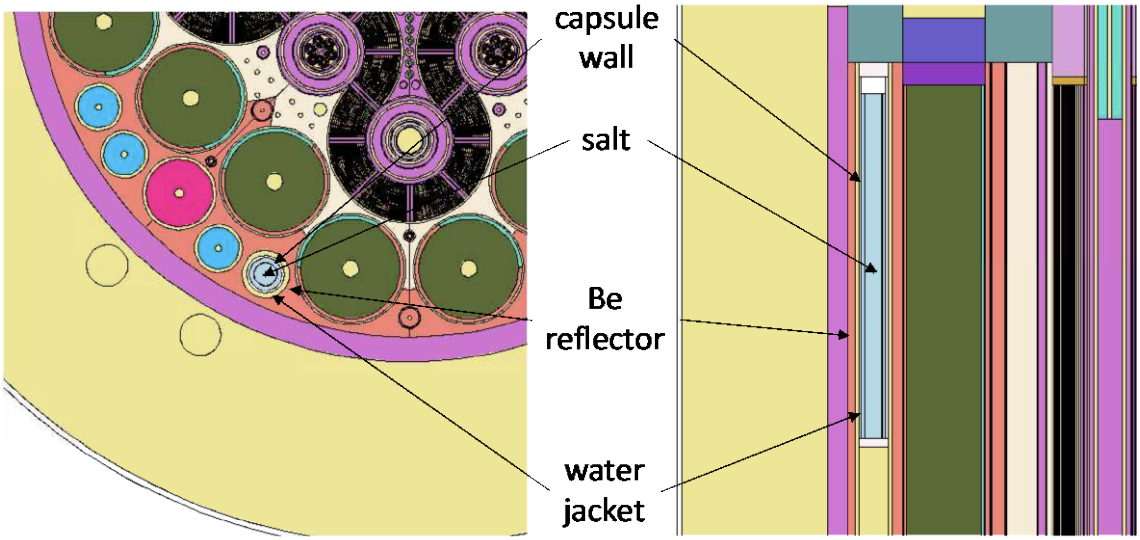

Figure 3. Cross-sectional views of the ATR MNCP6 model showing the VESIL experiment explicitly modeled in the I-9 position. The salt is shown in light blue.

While VESIL is envisaged to be able to test any type of salt composition (as long as appropriate safety considerations are accounted for), chloride salts were chosen for this analysis due to the notable lack of irradiation data compared to fluoride salts. As shown in Table II, multiple circulating in-pile experiments have been historically conducted on fluoride compounds. Chloride salts are therefore strong initial candidates for VESIL in light of industry interest, and greater uncertainty in their irradiation behavior.

These types of salts are primarily pursued by fast-spectrum reactors, because of their low moderating power (compared to fluoride compounds) and higher actinide solubility limits. Nevertheless, it is expected that irradiation in a thermal reactor such as the ATR would still be invaluable, as fission reactions (and the resulting products) are anticipated to be the main drivers of changes in chemical behavior. For instance, corrosion is anticipated to be primarily driven by fission product concentrations, rather than neutron damage.

A binary salt composition of UCl_3-NaCl was selected for the analysis. More specifically, a molar fraction of 45% UCl_3 – 55% NaCl, based on a concept in the literature [20], was used. Ternary salt containing UCl_4 was avoided due to its corrosive properties making it less desirable for an MSR concept. While some quantity of UCl_4 is expected to be unavoidably formed in the system, neutronic behavior is mainly driven by the initial UCl_3 concentration in the experiment.

Flux and power generation were tallied separately in the riser and downcomer channels of VESIL. Spatial self-shielding effect within the two channels was found to impact the overall thermal-hydraulic performance of the experiment. Each channel was therefore tallied separately to account for the large changes in power generation between them. Using an averaged power distribution did not correctly capture the resulting flow and temperature distribution in the experiment. Differences in the neutron spectra between the two regions are highlighted in Figure 4.

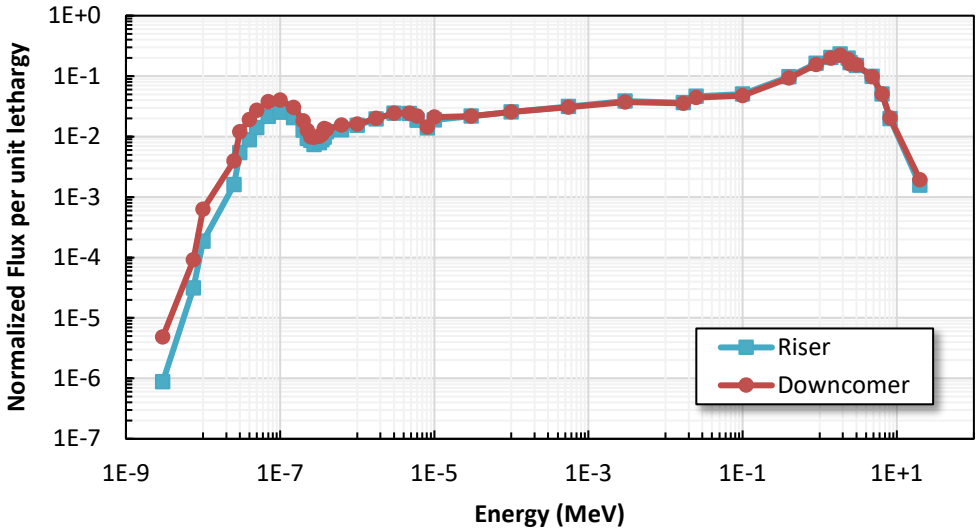

Figure 4. Normalized spectra in the riser and downcomer channels of the VESIL experiment.

The heat generation from neutron heating, fission reactions, and gamma heating were then tallied and used as inputs for the thermal-hydraulic model. The overall

contribution of different heating sources for an example iteration of the VESIL design is plotted in Figure 5.

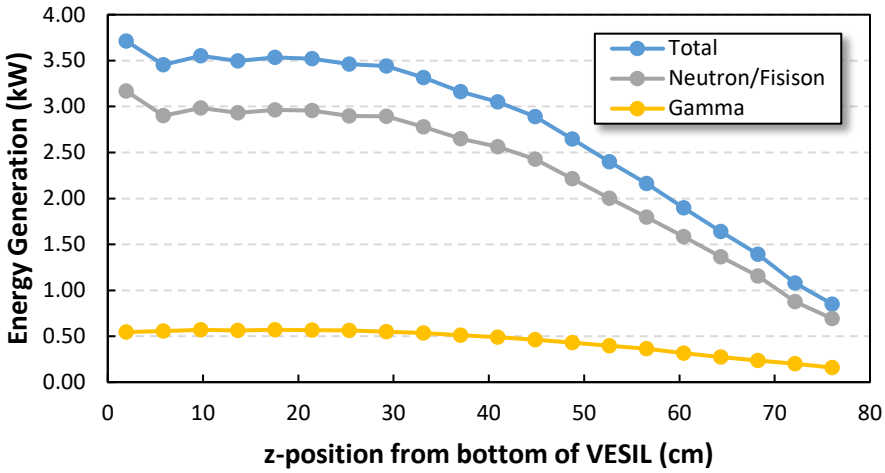

Figure 5. Neutron- vs. gamma-based contribution to heat generation inside VESIL.

II.B. Thermal-Hydraulic Model

II.B.1. 1-D System Code Model

The System Analysis Module (SAM) under development at Argonne National Laboratory is a 1-D systems code for advanced reactor analysis. SAM incorporates advances in physical modeling, numerical methods, and software engineering in order to enhance the user experience in simulating steady-state and transient problems. The tool is built on the object-oriented application framework MOOSE (Multiphysics Object-Oriented Simulation Environment) [21] and utilizes high-order spatial and time discretization schemes to solve 1-D fluid flow and heat transfer problems [22]. A system code was needed for this analysis, due to the complexities associated with analytically accounting for axial natural circulation and radial thermal conduction simultaneously. The tool also provides the flexibility to iterate on the geometrical and

thermal-hydraulic parameters in order to estimate the feasibility of a natural-circulation salt irradiation test loop in the ATR while incurring minimal computational costs.

VESIL was modeled using a combination of 1-D fluid-containing "component" and heat structures to represent the various flow paths and heat transfer. The model primarily consists of two 1-D channels: one for the riser and another to represent the downcomer. The SAM pipe component simulates 1-D fluid flow in two pipes linked together in a loop, as illustrated in Figure 6. Different components in the model were connected by junctions or branches. The baffle separating the two channels was modeled as a heat structure to account for the heat transfer between them. A fixed temperature boundary condition at the outside wall accounted for heat rejection to the ATR coolant.

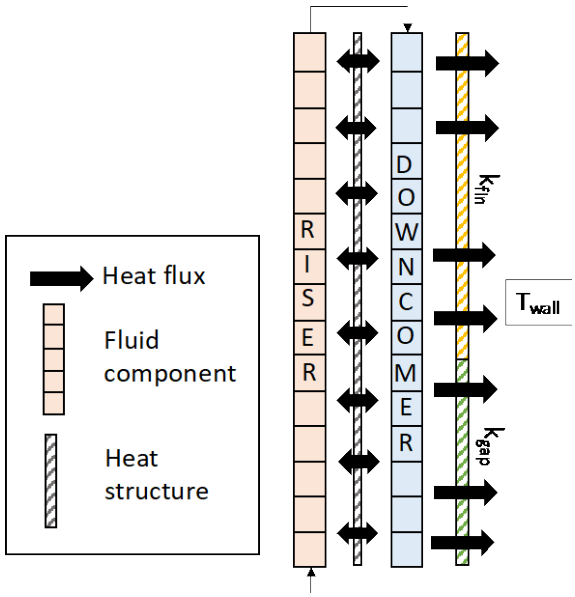

Figure 6. Schematic of the VESIL model simulated in SAM. Thermal communication between the two channels (via the baffle) is enabled.

The thermal properties of the salt were based on values found in the open literature for chloride-based salts. The density of the salt is expressed as a linear function of temperature, taken from [23]. Due to the lack of available literature on UCl_3-NaCl, all other thermal properties were assumed constant and were based on those

of another chloride-based salt, bearing the chemical composition 5% $PuCl_3$ – 42% UCl_3 – 52% NaCl [24]. The thermophysical properties are summarized in Table III.

Table III. Summary of thermophysical salt properties selected/assumed for this analysis.

Parameter	Value	Unit	Reference
Density (ρ)	3860.40–0.84T (K)	kg/m^3	[23]
Specific Heat Capacity (C_p)	9.50×10^2	J/(kgK)	[24]
Dynamic Viscosity (μ)	2.17×10^{-3}	kg/(ms)	[24]
Thermal Expansion Coefficient (β)	2.69×10^{-4}	K^{-1}	[24]
Thermal Conductivity (k_T)	7.00×10^{-1}	W/(mK)	[24]
Prandtl Number (Pr)	2.94	n/a	[24]

The model setup was verified against a 2-D computational fluid dynamics simulation using the commercial STAR-CCM+ code. The results showed good agreement in the maximum/minimum temperatures (within 1%) and induced natural-circulation velocity (within 2%) [25]. Following this verification, the SAM code was primarily used moving forward, in light of its significantly reduced computational expense.

A constant temperature boundary condition was applied at the VESIL outer wall. This was found to be a suitable assumption in light of the limited power generation in the experiment. Most VESIL design iterations generated power in the range of ~50 kW. Considering the I-9 experiment position and a VESIL outer-wall diameter of 8.25 cm, the ATR coolant mass flow rate ($\dot{m}$) through the external water jacket can be estimated using:

$$\dot{m} = 236 \times D_{eff}^2 \times \sqrt{\frac{\Delta P}{K\rho}} \quad (1)$$

where D_{eff} is the effective diameter defined by the ratio between the inner- and outer-annulus flow area diameters, ΔP is the pressure drop through the ATR core, ρ is water coolant density, and K is the resistance coefficient estimated using the Moody chart. This results in a 41 kg/s mass flow rate through the annular water jacket. The temperature rise across the jacket (ΔT) can then be estimated using:

$$Q = \dot{m} C_p \Delta T \tag{2}$$

For an experiment heat generation (Q) of 55 kW, the water coolant rises a mere 0.3 K across the channel. This validates the constant boundary temperature assumption in the SAM model.

While the ATR coolant inlet/outlet temperature remains relatively constant, a simple convection model was used to determine a representative wall temperature as a boundary condition in the SAM model. Using the Dittus-Boelter correlation from Equation 3, the Nusselt number (Nu) could be estimated. In this equation, Re is the Reynold's number and Pr the Prandtl number. With an Re value comfortably above the 10,000 limit, and a length-to-diameter ratio above the 10 limit, the correlation is determined to be applicable for usage here.

$$Nu = 0.023 \times Re^{0.8} \times Pr^{0.33} \tag{3}$$

A heat transfer coefficient (h) of 57.5 kW/m^2-K was estimated. The resulting wall temperature (T_w) could then be evaluated using:

$$Q = h\, A\, (T_w - T_b) \tag{4}$$

where A is the heat transfer area and T_b is the bulk coolant temperature. A temperature rise of 3 K was calculated, and an experiment wall boundary condition of 56°C was applied as a result.

II.B.2. Analytical Model for Thermal Conduction

To control the heat flux to the ATR coolant and drive a temperature gradient, two separate heat conduction systems were relied on. One utilizes different gas mixtures to inhibit heat flux to the outside, while the other uses fins to fine-tune the heat transfer. The latter is a novel approach under development at INL to achieve heat transfer goals in high-power density experiments [26]. Advanced manufacturing (most notably, 3-D printing) can be used to create a circular finned pattern using a wide range of materials, including aluminum, magnesium, copper, carbon steels, and even graphite. An illustration of the fin-gap is provided in Figure 7.

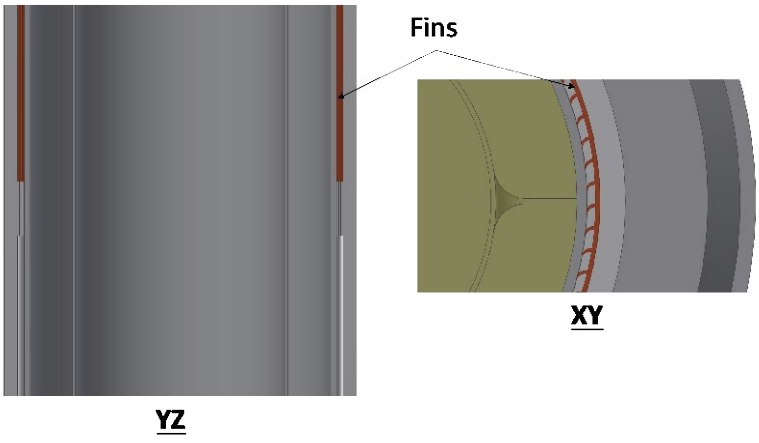

Figure 7. Cross-sectional views of VESIL showing the fin-gap in red.

Both the gas-gap and fin-gap can then be fine-tuned to reach a desired equivalent heat conduction coefficient. For the gas-gap, this is accomplished mainly by increasing/decreasing the gap thickness and manipulating the gas mixture (He/Ne/Ar); and for the fin-gap, by customizing the number, material, and dimensions of the fins.

The equivalent thermal conductivity for the gas-gap (k_{gap}) is then calculated using:

$$k_{gap} = \frac{\ln(\frac{r_4}{r_1})}{\frac{\ln(\frac{r_2}{r_1})}{k_{SS}} + \frac{\ln(\frac{r_3}{r_2})}{k_{gas}} + \frac{\ln(\frac{r_4}{r_3})}{k_{SS}}} \quad (5)$$

The radii, r_1 to r_4, corresponds to the inner salt wall, the salt wall thickness, the gap radius, and the outer wall of VESIL respectively. k_{SS} is the conductivity of Stainless Steel 316, the assumed wall material for VESIL. The gas thermal conductivity k_{gas} is based on the He/Ar gas ratio. It can be modified even during irradiation by injecting one of the gases to tailor the ratio to specific temperature targets.

Two key factors played a role in the selection of the VESIL fin material: (1) melting temperature and (2) safety of incorporating that fin material into the ATR. Structural material properties were not prioritized as the fins only need to ensure good contact between the two walls. With those factors in mind, copper was chosen as the fin material for this preliminary study. Copper's melting temperature of 1358 K is higher than the operating temperature of VESIL, thereby affording the required safety margin. The high thermal conductivity of the material also corresponds with increased heat transfer to the ATR coolant, ultimately increasing the natural-circulation velocity. The fins run from the top of the salt in VESIL to near its middle, with the rest of the length occupied by the gas-gap mixture. Equivalent thermal conductivity of the fin-gap (k_{fin}) is estimated by summing the various thermal resistances as follows:

$$k_{fin} = \frac{\ln\left(\frac{r_{out}}{r_{in}}\right)}{2\pi(R_{wall1}+R_{cont}+R_{fin}+R_{insert}+R_{interf}+R_{wall2})} \quad (6)$$

The resistivity of the two capsule walls (R_{wall1} and R_{wall2}), as well as that of the radial insert (R_{insert}), are computed in similar fashion to Equation 5, using: $\frac{\ln(\frac{r_2}{r_1})}{k_{SS}}$. The

fin contact resistance (R_{cont}) is estimated using Equation 7. It is expressed as a function of the number of fins (N_{fin}), the contact length (L_{cont}), the fin thickness (t_{fin}), and the contact heat transfer coefficient (h_{cont}). Fin resistance (R_{fin}) is computed using Equation 8, where L_{fin} is the total length of the fin and k_{fm} is the fin material's thermal conductivity. Lastly, resistance between the insert and the outer VESIL wall (R_{interf}) is computed using Equation 9. r_{ins} is the insert radius, while h_{interf} is the insert-wall contact heat transfer coefficient.

$$R_{cont} = \frac{L_{cont} \times N_{fin}}{\frac{k_{gas}}{t_{fin}} + h_{cont}} \tag{7}$$

$$R_{fin} = \frac{L_{fin}}{k_{fm} \times t_{fin} \times N_{fin}} \tag{8}$$

$$R_{interf} = \frac{1}{2\pi\, r_{ins}\, h_{interf}} \tag{9}$$

II.C. Species Mass Transport Model

A particularly valuable aspect of this experiment is the online analysis of fuel salt burnup using a helium gas sparging system to extract insoluble fission products (IFPs) to an off-gas system. To determine the feasibility of such a design, a species mass transport model must be utilized. By tracking the spatial distribution of insoluble species, the burnup process, along with dynamic fission product behavior, can be better understood and exploited for experimental purposes in the loop design. Through work carried out at Oak Ridge National Laboratory, the subchannel thermal-hydraulics code CTF (COBRA-TF) was modified to incorporate a general species transport model and a simple helium bubble transport model [27]. This general species transport framework was utilized and enhanced to incorporate noble metal (NM) transport and deposition on

surfaces as well as to include extraction via helium bubbles to analyze the off-gas extraction mechanism proposed for VESIL [28].

This work utilizes the framework built into CTF for tracking several highly radioactive isotopes of interest that are expected to be extracted into the off-gas system in VESIL and assess the resulting source-term/decay heat present in such a system. Additionally, NM deposition on surfaces in VESIL is examined—specifically Te, an important chemical species to track, due to its role in corrosion [29]. A detailed analysis of the helium bubble and thin film mass transfer models was given in [28]. Below is a general description of the species transport model.

II.C.1. General Species Transport Equations

The general species transport partial differential equation implemented into CTF in a non-discretized form is given as [30]:

$$\frac{\partial \rho_a^{(b)}}{\partial t} = -\nabla \cdot \left(\rho_a^{(b)} \vec{v}\right) + S \tag{10}$$

The terms, from left to right, include the change in the mass density of a certain species (subscript a) in a given mass transport regime (superscript b) with respect to time, advective mass transport of the species due to a velocity field, all the associated loss and gain terms from species radioactive decay, and regime changes from mass transfer mechanisms. The diffusion mechanism is assumed to be negligible relative to the flow rate, but it is incorporated in determining the mass transfer coefficient as species leave the 1D bulk flow and deposit on surfaces in the experiment. Using the example of the Sb → Te decay chain in three transport regimes (superscripts bl, ss, and gs) yields Equations 11–16. Here, the transport regimes describe how the species is being transported and where it is currently located: directly dispersed in the bulk liquid

(superscript *bl*) (Equations 11 and 14), immobile on a structural surface (superscript *ss*) (Equations 12 and 15), or transported by a bubble/gaseous surface (superscript *gs*) (Equations 13 and 16). It is important to note that the $\vec{v}$ term is bulk liquid velocity and it is the same for species in the bulk liquid (superscript *bl*) and for the species attached to helium bubble surfaces (superscript *gs*) since the helium bubbles are modelled as an homogenous equilibrium two phase flow where there is no phasic slip between the bubbles and the bulk liquid flow [30]. Lastly, the *K* and *A* values in the deposition terms are the mass transfer coefficients and surface areas available for deposition and the method for calculation is shown in [30].

$$\frac{\partial \rho_{Sb}^{(bl)}}{\partial t} = -\nabla \cdot \left(\rho_{Sb}^{(bl)} \vec{v}\right) + \frac{M_{Sb}}{N_A} \gamma_{Sb} \Sigma_f \phi - \lambda_{Sb} \rho_{Sb}^{(bl)} - \frac{K_{ss} A_{ss}}{V_{cell}} \rho_{Sb}^{(bl)} - \frac{K_{gs} A_{gs}}{V_{cell}} \rho_{Sb}^{(bl)} - \sigma_{a_{Sb}} \phi \rho_{Sb}^{(bl)} \tag{11}$$

$$\frac{\partial \rho_{Sb}^{(ss)}}{\partial t} = \frac{K_{ss} A_{ss}}{V_{cell}} \rho_{Sb}^{(bl)} - \lambda_{Sb} \rho_{Sb}^{(ss)} - \sigma_{a_{Sb}} \phi \rho_{Sb}^{(ss)} \tag{12}$$

$$\frac{\partial \rho_{Sb}^{(gs)}}{\partial t} = -\nabla \cdot \left(\rho_{Sb}^{(gs)} \vec{v}\right) + \frac{K_{gs} A_{gs}}{V_{cell}} \rho_{Sb}^{(bl)} - \lambda_{Sb} \rho_{Sb}^{(gs)} - \sigma_{a_{Sb}} \phi \rho_{Sb}^{(gs)} \tag{13}$$

$$\frac{\partial \rho_{Te}^{(bl)}}{\partial t} = -\nabla \cdot \left(\rho_{Te}^{(bl)} \vec{v}\right) + \frac{M_{Te}}{N_A} \gamma_{Te} \Sigma_f \phi + \frac{M_{Te}}{M_{Sb}} \lambda_{Sb} \rho_{Sb}^{(bl)} - \lambda_{Te} \rho_{Te}^{(bl)} - \frac{K_{ss} A_{ss}}{V_{cell}} \rho_{Te}^{(bl)} - \frac{K_{gs} A_{gs}}{V_{cell}} \rho_{Te}^{(bl)} - \sigma_{a_{Te}} \phi \rho_{Te}^{(bl)} \tag{14}$$

$$\frac{\partial \rho_{Te}^{(ss)}}{\partial t} = \frac{K_{ss} A_{ss}}{V_{cell}} \rho_{Te}^{(bl)} + \frac{M_{Te}}{M_{Sb}} \lambda_{Sb} \rho_{Sb}^{(ss)} - \lambda_{Te} \rho_{Te}^{(ss)} - \sigma_{a_{Te}} \phi \rho_{Te}^{(ss)} \tag{15}$$

$$\frac{\partial \rho_{Te}^{(gs)}}{\partial t} = -\nabla \cdot \left(\rho_{Te}^{(gs)} \vec{v}\right) + \frac{K_{gs} A_{gs}}{V_{cell}} \rho_{Te}^{(bl)} + \frac{M_{Te}}{M_{Sb}} \lambda_{Sb} \rho_{Sb}^{(gs)} - \lambda_{Te} \rho_{Te}^{(gs)} - \sigma_{a_{Te}} \phi \rho_{Te}^{(gs)} \tag{16}$$

Taking Equation 14 as an example, the terms (starting from the left) include the change in $\rho_{Te}^{(bl)}$ with respect to time, the advection of $\rho_{Te}^{(bl)}$ by the velocity field, the constant generation term for $\rho_{Te}^{(bl)}$ from fission in that cell, the gain term from the decay of $\rho_{Sb}^{(bl)}$the loss term from the decay of $\rho_{Te}^{(bl)}$ to its daughter species, loss of $\rho_{Te}^{(bl)}$ due to

mass transfer to wall surfaces in the experiment, and loss of $\rho_{Te}^{(bl)}$ due to mass transfer to gaseous bubbles in the experiment, and loss of $\rho_{Te}^{(bl)}$ via transmutation due to neutron absorption.

Isotopes tracked are born from fission in the bulk liquid (*bl*) regime, then decay to other species or mass transfer to other regimes in which the species are continually tracked. The color-coded terms show the relation between the differential equations, how the mass transfer mechanisms track the regime changes of a certain isotope, and how the decay terms track the loss of isotopes in each regime to its daughter product. The neutron absorption loss term is included for species when it becomes significant in relation to the other source terms—most notably ^{135}Xe, with its large thermal neutron cross section. The one-group cross sections are tallied directly from the MCNP6 model in Section II.A.

II.C.2. CTF Geometry

The equivalent CTF geometry shown in Figure 8 is a simple 1-D loop to enable time-dependent and steady-state calculations for species build-up and transport during the 60-day irradiation. It is subdivided into eight cells that communicate with adjacent ones and allow for species transfer. The fission product generation rate is based on the power distribution calculated via MCNP6, and the mass transfer rate is a function of the flow field and geometry of the surface-to-volume ratio in each cell. Most fission products are generated in the lower sections of VESIL where the thermal flux is highest. The helium sparging system is implemented at cell #1, and the bubbles flow concurrently up through the inner riser, where they are then extracted in cell #5 across the liquid-gas interface and over to the off-gas system.

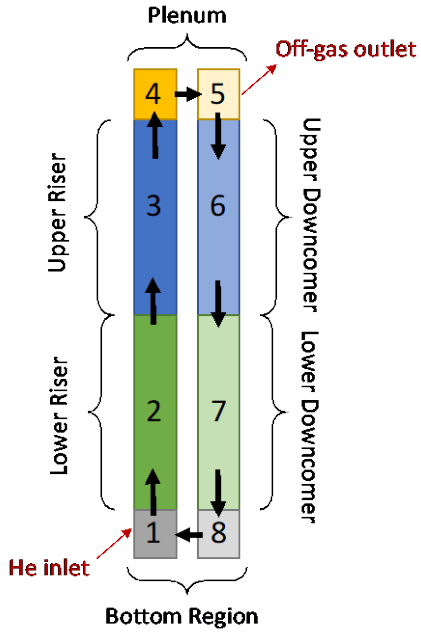

Figure 8. Equivalent VESIL geometry in CTF, highlighting the eight cells in which species are tracked.

The rate of bubble extraction for cell #5 is an input parameter in the current species transport model, and it is assumed that this helium gas sparging system parameter can be forced with specific engineering considerations (e.g., bubble-size control, a baffle for bubble extraction, etc.). Further higher-fidelity modeling (e.g., two-phase computational fluid dynamics) would be needed to understand the bubble interactions in light of these engineering considerations, along with a thermal-hydraulic mock-up to accurately predict and demonstrate the ability to control the size and general behavior of bubbles in the experiment.

II.D. Analysis Pathway

Once the different models were set up, an iterative approach was followed to optimize the design and identify feasible variants. A flow chart illustration of the various steps is provided in Figure 9, giving a high-level overview of the logical path followed as part of the design iteration approach.

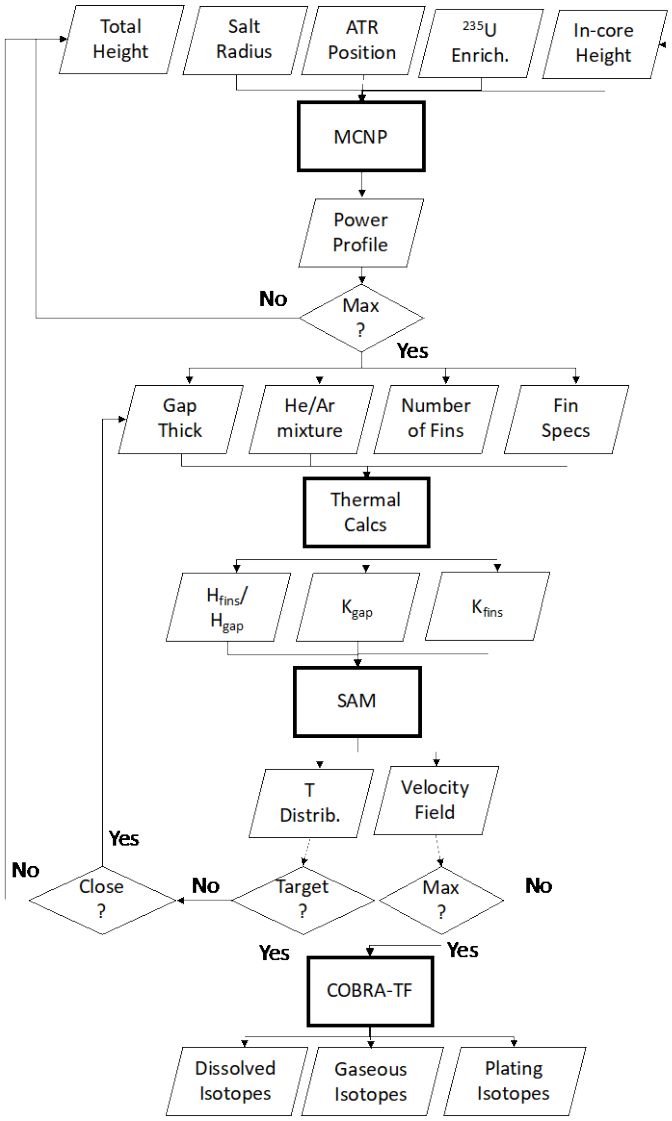

Figure 9. Flow chart of the iteration scheme followed to optimize the main design parameters of VESIL.

The analysis is divided into four main steps: (1) neutron transport simulation using MCNP, (2) iteration over the thermal calculations from Equations 5 and 6, (3) thermal-hydraulic simulation in SAM, and (4) species mass transport using the modified version of CTF. The different steps are approached in series, with each step providing the necessary inputs for the next. Previous parametric evaluations contributed to slightly narrowing the range of variables considered [25].

The primary input for Step 1 includes the VESIL dimensions along with the distance of its axial insertion into the core (as a function of the top of the ATR fuel

meat). Different values can be iterated upon to reach a suitable heat generation profile. Uranium enrichment was also considered, but it was quickly decided to maximize it to the high-assay low-enriched uranium limit of 19.75 wt% in order to maximize power generation. High-enriched uranium was not considered due to additional requirements that would be imposed on the experiment from a safeguard and security perspective. Similarly, although a large I-position was initially considered, a medium I-position was settled upon due to its higher flux and sufficient volume. The main output from Step 1 is a heat generation distribution (for both the riser and downcomer channels of VESIL) fed into the thermal-hydraulic model.

Once a power profile is obtained, the next step is to generate equivalent thermal conductivities for the gas-gap and fin-gap. These equivalent conductivities are then fed into the SAM model in Step 3, along with the MCNP-produced heat generation distribution and selected fin-height-to-gas-height ratio of the gaps. The outputs are a temperature distribution along VESIL and a peak natural-circulation velocity. The resulting velocity distribution is believed to be conservative as it does not account for flow induced by helium bubbling in the system. If the resulting temperature distribution is within the range of interest for the MSR community, and the velocity is above a minimum threshold of 0.1 m/s, the analysis moves forward to the next stage. Otherwise, the thermal conductivities are modified, and the same stage of analysis repeated. If the evaluation still cannot satisfy the temperature and velocity criteria, the inputs to the MCNP model (e.g., insertion height into the core) are revisited.

Lastly, once a design is settled upon, a final evaluation of the fission product distribution is conducted using a species mass transport tool built into CTF. This provides first-order estimates of the quantities of certain isotopes expected to be observed during irradiation of the VESIL experiment.

The following section provides an overview of the main iteration steps and the required conditions satisfied by characteristics of the preliminary VESIL design. For the sake of brevity, although multiple parametric iterations were conducted, Section III highlights only the most relevant cases.

III. ASSESSMENT OF EXPERIMENT DESIGN PARAMETERS

III.A. Parametric Evaluation of Heat Generation

The main objective of the MCNP simulation is to maximize heat generation within VESIL. However, in some instances, this conflicts with maximizing velocity (if the power profile is too uniform across the loop) or the targeted temperature gradients (if enough heat cannot be emitted using a realistic number of fins). Generally, heat generation is an important driver for the temperature gradient within the salt, hence density change, and hence the salt flow rate. As a result, the analysis will aim to maximize the power density within VESIL.

Opting for a large I-position rather than a medium I-position reduced the total power generation within VESIL by 30.9% while holding all other parameters constant. In addition, since the medium I-position was shown in Section II.B.1 to allow sufficient cooling volume, this position (more specifically, I-9) was selected to be modeled in the analysis moving forward. Similarly, the uranium enrichment was fixed at 19.75 wt% to maximize the rate of fission reactions as previously specified.

Following parametric evaluations, a salt radius of around 2.7 cm was found to be ideal from a frictional-loss standpoint, along with a total height of 78 cm [25]. As a result, the main variable to investigate via the MCNP simulation is the axial insertion height of VESIL into the core. A parametric evaluation of this variable is plotted in

Figure 10 for different axial slices along the height of VESIL. The results are summed for both the downcomer and riser regions.

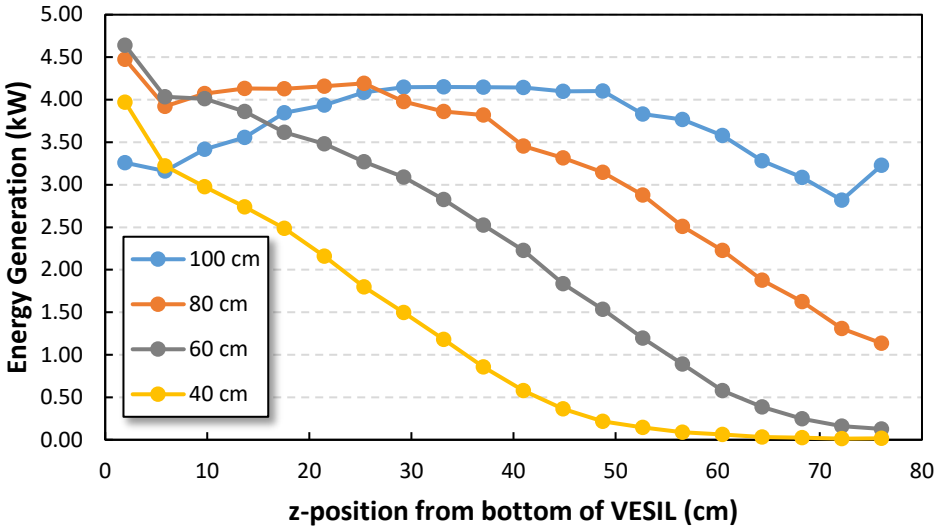

Figure 10. Evolution of the power distribution in VESIL as a function of its axial insertion height into the ATR. The average Monte Carlo standard deviation in each axial slice was 2.7%.

A spike in power due to incoming thermalized neutrons from both the radial and axial directions was observed at the very bottom of VESIL. Ideally, both the total heat generation and peak power density would be maximized in this step. As shown in Figure 11, this would correspond to an insertion between 60-100 cm insertion into the core. However, subsequent thermal analysis found that configuration with around 80 cm insertion struggled to maximize the natural-circulation velocity, mostly because the relatively symmetric power distribution observed in Figure 10 did not lend itself to driving a large temperature gradient across VESIL.

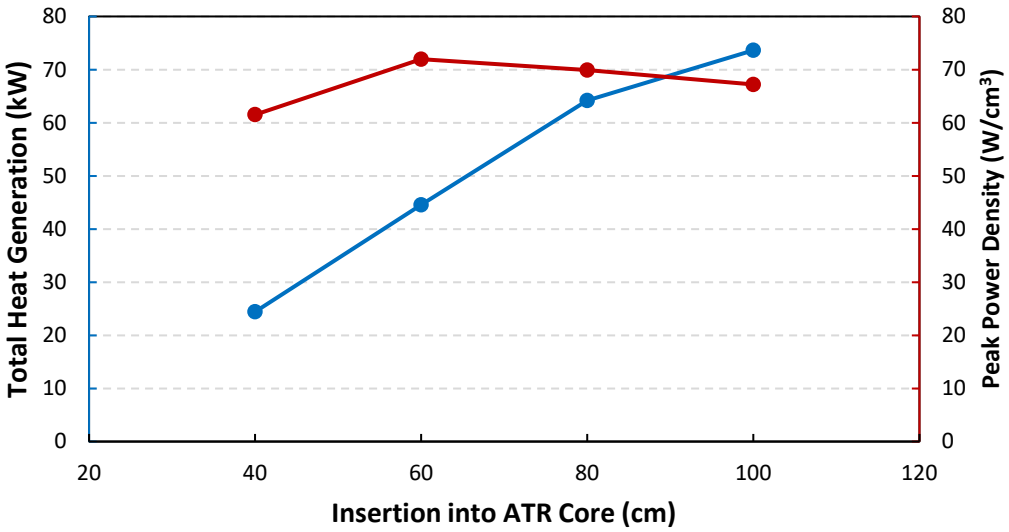

Figure 11. Evolution of total heat generation and peak power density against the insertion height in the ATR core.

As a result, the 60-cm insertion was favored for the final design. This corresponds to a total power generation of 44.45 kW in VESIL. The equivalent burnup after one ATR cycle, averaged over the salt would be 0.7 GWd/MTU (assuming constant power generation throughout the cycle). While the power density in the experiment would peak at 72 W/cm^3, the relatively large salt volume dilutes the overall burnup. The power density in each region is plotted in Figure 12 and used as an input to the thermal analysis in Section III.B.

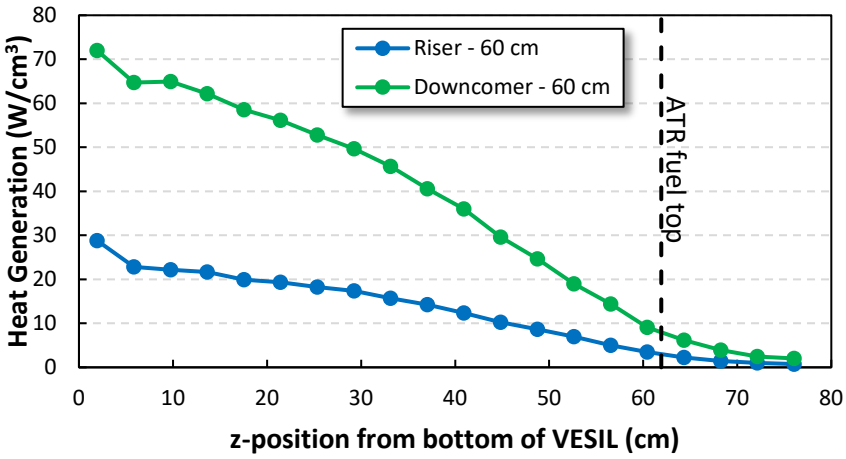

Figure 12. Comparison of the power density in the riser and downcomer regions of VESIL for a 60-cm insertion in the ATR core.

III.B. Optimization of Temperature and Velocity Distribution

Multiple iterations on the values of k_{gap} and k_{fin}, along with their corresponding heights, were conducted to reach the desired maximum temperature of 670°C (based on [24]). Figure 13 showcases the various cases considered. They are plotted against the weighted ratio of the length by the thermal conductivity of the fin and the gap region. This provides a useful design metric that has a strong impact on the temperature gradient of the system. Flow reversals were observed when the fin height comprised more than 60% of the total VESIL height and its equivalent thermal conductivity was relatively elevated. Many iterations reached peak temperature exceeding material limits and are therefore infeasible.

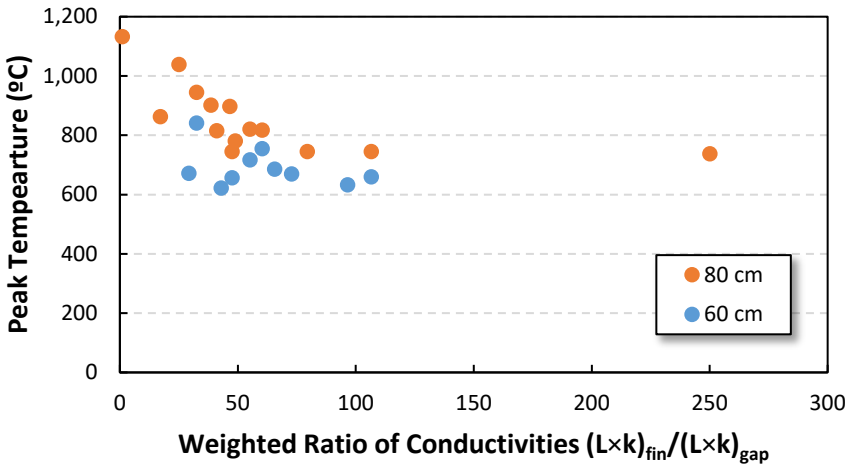

Figure 13. Iterations of the conductivity and relative height of the gas-gap and fin-gap regions to reach a targeted peak temperature.

With fin-gap and gas-gap equivalent thermal conductivities of 11.13 W/m-K and 0.27 W/m-K, respectively, a maximum temperature of 670°C can be reached, as shown in Figure 14. The fin-gap length was set to 50 cm, while the gas-gap length was 28 cm. The peak velocity induced by natural circulation was 0.15 m/s.

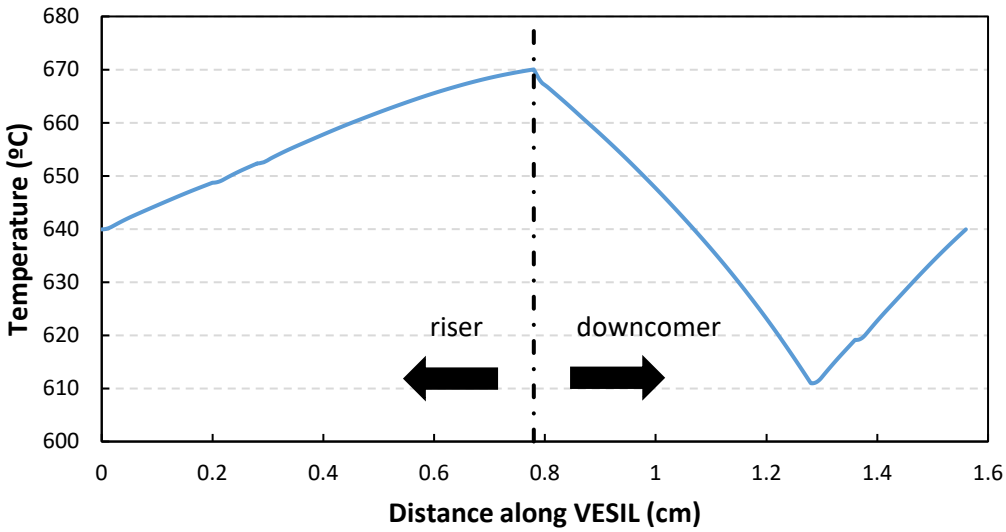

Figure 14. Temperature distribution along the length of VESIL.

The conceptual design specifications for VESIL are summarized in Table IV. The analysis demonstrated the feasibility of a relatively compact (less than 10 kg of salt) model that can reach a targeted temperature range relevant to the MSR community and generate natural circulation of 0.15 m/s. Though the temperature gradients and velocity fields are lower than those in some proposed concepts (see [20][24]), they are still expected to be useful for an initial experiment and to provide validation data for models. Reaching more representative flow characteristics will require development and qualification of a forced flow system that can survive the ATR's irradiation environment. This is expected to be substantially more expensive than the current scope of VESIL, along with a noted increase in development-related risk.

Table IV. Dimensions and specifications of the conceptual VESIL design.

Parameter	Value
Outer radius (cm)	3.25
Salt/downcomer radius (cm)	2.78
Salt height (cm)	78.00

Riser flow area (cm^2)	11.81
Downcomer flow area (cm^2)	11.81
Total salt mass (kg)	6.36
k_{gap} (W/m-K)	0.27
k_{fin} (W/m-K)	11.13
Gas-gap height (cm)	28.00
Fin-gap height (cm)	50.00
Insertion height in the ATR core (cm)	60.00
Total heat generation (kW)	44.54
Peak power density (W/cm^3)	71.96
Salt max. temperature (°C)	670.03
Salt ΔT (K)	59.04
Salt peak velocity (m/s)	0.15

To reach the desired equivalent thermal conductivities, the fin-gap and gas-gap dimensions and characteristics must be fine-tuned, as explained in Section II.B.2. Table V summarizes the specifications needed for meeting the values shown in Table IV. Following a review by experts at INL, these parameters are considered manageable from a manufacturing standpoint.

Table V. Specifications for the gas-gap and fin-gap to reach the targeted equivalent thermal conductivities.

Parameter	**Value**
Gas-gap thickness (cm)	0.125
He/Ar ratio	25/75
Salt wall thickness (cm)	0.100

Outer wall thickness (cm)	0.247
Number of fins	85
Fin thickness (cm)	0.030
Fin length (cm)	0.150
Fin contact length (cm)	0.050
Fin insert thickness (cm)	0.085

1

2 **III.C. Overview of Preliminary Engineering Design**

3 As final verification of the feasibility of the VESIL design specification,
4 preconceptual engineering drawings were generated. These computer-aided design
5 (CAD) models are shown in Figure 15 and Figure 16. A handle is included to position
6 the experiment in the required location in the ATR. Fixtures are included to stabilize the
7 structure mechanically and help alleviate potential flow-induced vibrations. Two sets of
8 gas lead-outs are needed in the model: one for the off-gas and another to control the
9 gas-gap mixture. Additional lead-outs for electrical wirings are included as well.

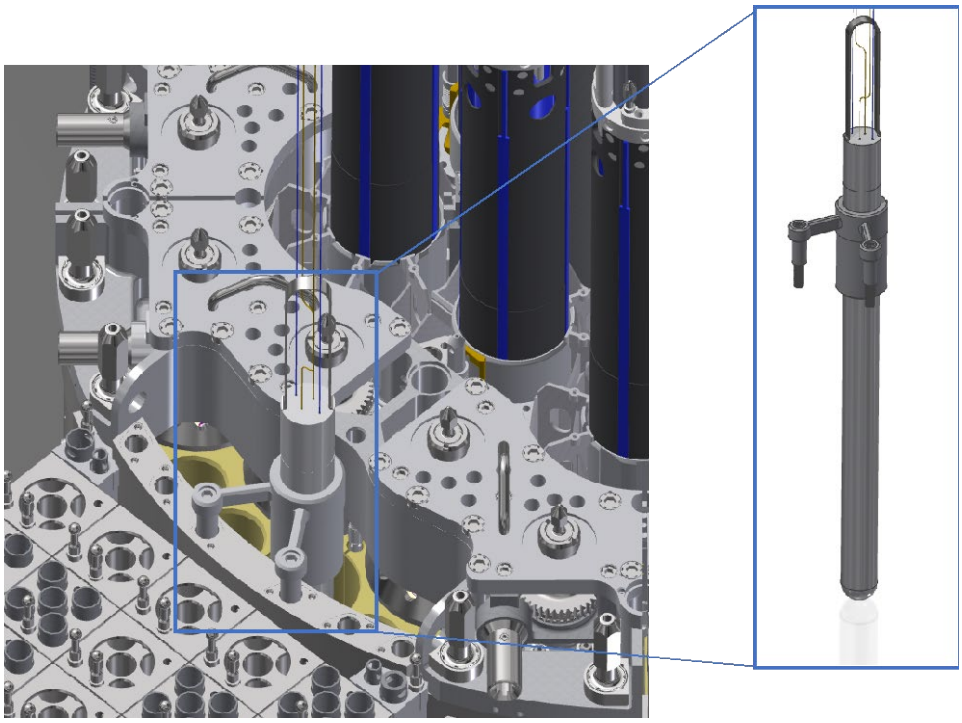

Figure 15. Illustration of the VESIL experiment inside the ATR.

The cut-out view of Figure 16 illustrates the VESIL internals. One off-gas line is directed to the very bottom of the loop to provide helium bubbling for assisting in the evacuation of the generated fission gases (discussed in Section II.C) and driving the off-gas flow. The second off-gas line runs from the top of the VESIL gas plenum and flows gas out of the system. The two salt channels are separated by a baffle suspended in the salt bath. Small separating ridges (not shown in the cross-sectional view) force the gas-gap thickness and fix the internal salt wall. The fin insert rests on these ridges, also ensuring they are fixed in place.

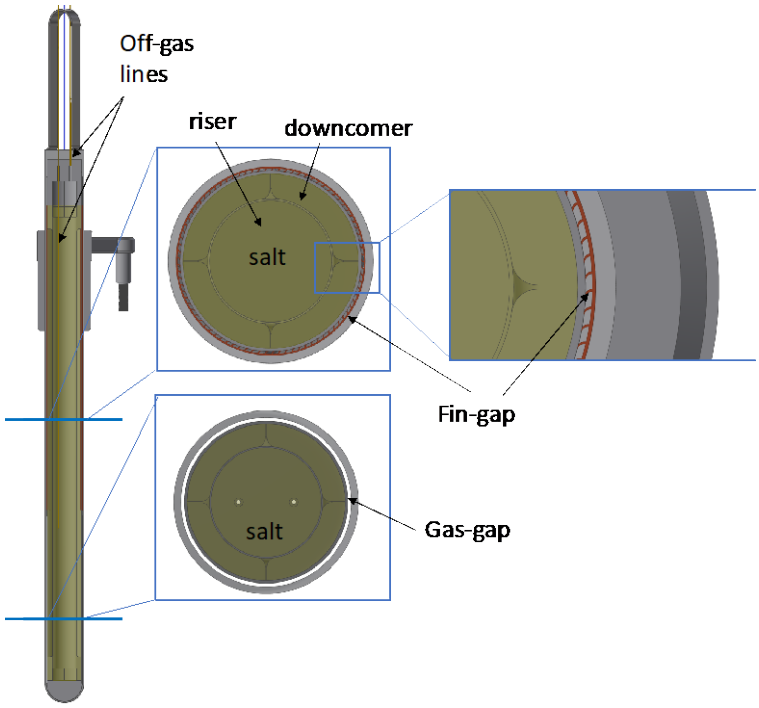

Figure 16. Cut-out view of VESIL highlighting the fin-gap and gas-gap regions.

An investigation of the outer wall thickness was conducted to verify the feasibility of the proposed design. The main purpose was to ensure that the selected thickness was adequate to withstand the reactor pressure. For conservatism, the internal VESIL pressure is assumed to be near atmospheric (in reality, the gas-gap mixture will be slightly pressurized). Also, no credit is given to the fins and wall rivets for providing some support on the compression strains acting on the outer capsule wall. The (conservative) maximum allowable pressure (P_{max}) for the given conditions is calculated using the following ASME (American Society of Mechanical Engineers) standard relation [31]:

$$P_{max} = \frac{4B}{3(D_o/t)} \tag{10}$$

where D_o/t corresponds to the outer-diameter-wall-to-wall-thickness ratio. The B factor is obtained using an ASME-provided chart. It is expressed as a function of the ratio of the length to the outer diameter (D_o/t) and the expected wall temperature. An estimated

maximum pressure of 3.9 MPa was calculated, which already provides a significant margin relative to the 2.7-MPa ATR operating pressure.

III.D. Additional Design Considerations

While the current analysis established the feasibility of the VESIL design using a first-order estimate, future work needs to address the safety basis for such an experiment prior to irradiation inside the ATR. This will include analysis and evaluation of various postulated accident scenarios, such as:

1. Leakage of salt into secondary containment will result in salt-freezing and potential radiolysis. The secondary wall must be able to withstand the resulting pressure increase.
2. Leakage of water into secondary containment will cause salt-freezing and radiolysis. Off-gas must be able to manage higher flow rates.
3. Simultaneous leakage in both walls could cause a salt-water thermochemical reaction. This is considered very unlikely, but evaluations should be conducted and potential mitigations implemented.
4. Leakage from the off-gas line will release radioactive material into the ATR coolant. Potential mitigation steps may be necessary to add an additional barrier to mitigate such release.
5. Flow blockage will result in decreased natural circulation. This could result in substantial rises in salt temperatures. Potential mitigations are to ensure that the salt wall can withstand very elevated temperatures, or to inject gas/liquid into the gap to increase thermal conductivity.

IV. SPECIES MASS TRANSPORT AND ACCOUNTANCY

Due to the dynamic fuel salt composition with the build-up of IFPs, the spatial

composition of several key species is tracked using the species transport model in CTF (described in Section II.C). With implementation of the gas sparging and off-gas systems, several IFPs will interact with the bubble swarm and be extracted for online analysis. Most notably, the NGs (Xe and Kr) and their subsequent daughter products will be extracted to the off-gas system. Additionally, it is anticipated from the MSRE experience that NMs will deposit on the gas-liquid interface of bubbles as well as on the open liquid-gas surface at the top of VESIL [32]. The majority of NMs will likely stay on this liquid-gas interface at the top of VESIL, but some may be swept into the off-gas system by the helium gas.

As a result, several key NG and NM decay chains are modeled, as seen below in Table VI. Here, blue represents an insoluble NG species, red represents an insoluble NM species, and green indicates a soluble species remaining in the fuel salt. The solubilities are based on fission product behavior during the MSRE [32].

Table VI. Decay chains tracked in this analysis.

Decay Chains Tracked by CTF								
^{141}Xe → … ^{141}Ce	^{140}Xe → … ^{140}La	^{139}I → … ^{139}Ba	^{138}Te → … ^{138}Cs	^{137}Te → … ^{137}Xe	^{136}Te → … ^{136}I	^{135}Sb → … ^{135}Xe	^{134}Sn → … ^{134}I	^{133}Sn → … ^{133}Xe

All the species in these decay chains must be tracked explicitly to account for their spatial distributions and behavior when decaying. As seen in ^{138}Te → ^{138}I → ^{138}Xe → ^{138}Cs, the species will change behavior as they progress down the decay chain, starting as a NM, becoming a soluble species, becoming an NG, and then becoming soluble again. Therefore, it is likely that small quantities of soluble Ce, La, Ba, and Cs

will be found in the off-gas system, due to the extraction of their Xe precursor. Additionally, if some NMs detach from the liquid-gas free surface and are swept into the off-gas system, then traces of I will also be present in the off-gas system.

Ideally, all decay chains containing NMs and NGs (Nb → In and Kr) should be tracked to give a more holistic calculation of all the species potentially extracted by the helium gas sparging. This preliminary analysis focuses on decay chains containing Xe and short-lived isotopes that will be in a steady-state spatial distribution by the end of the 60-day irradiation. It is a proof-of-concept calculation to aid in discussing the feasibility and utility of the current experimental design; namely, what sort of online fuel salt analysis is possible, what model development and/or thermal-hydraulic mock-up is required for helium-sparging, and which NM species plating distributions in the loop should be compared with a post-irradiation examination.

IV.A. Results of Species Mass Transport Analysis

As previously mentioned, this analysis is a steady-state calculation of the spatial distributions for those species shown in Table VI. It will be a close approximation, as the species asymptotically approach their steady-state distributions after 60 days of irradiation in the experiment. To demonstrate this, Table VII shows time-explicit calculations on the degree to which certain species will accumulate in the off-gas system as a percentage of their steady-state values in that system.

Table VII. Time-explicit steps showing the convergence of specific isotopes as a percentage of their steady-state concentration in the off-gas system.

	^{133}Sn	^{133}Sb	^{133}Te
$T_{1/2}$	1.46 s	2.50 m	12.5 m
t = 51.0 s	91.9%	2.53%	0.144%
t = 4.32 m	~100.0%	51.5%	7.07%

t = 8.63 m	~100.0%	84.8%	21.0%
t = 17.3 m	~100.0%	98.6%	45.1%

As seen above, the shorter the half-life, the quicker the species solution converges on the steady-state value. Since all the selected species have short half-lives much lower than the 60-day irradiation period, the ones considered will reach their steady-state spatial distribution within one ATR power cycle. A more complete and time-dependent analysis of long- and short-lived NMs and NGs is required for comparison with post-irradiation experiments; however, this initial analysis is useful in determining the feasibility of a helium sparging off-gas extraction system for online analysis.

IV.A.1. Effect of Varying Bubble Removal Rates on IFP Extraction

For a concurrent bubble-liquid flow design, two extreme cases are possible in implementing the helium bubble sparging system. One is that the effect of buoyancy will be significant in creating a phasic slip velocity, or the introduction of a baffle will ensure that the extraction rate of bubbles from VESIL to the off-gas system is significant. Another option is to maintain a small enough bubble size to avoid significant phasic slip, while also controlling the extraction rate to the open liquid-gas interface that will be limited by diffusion, resulting in significant bubble recirculation in VESIL. Since this is a rudimentary analysis, both cases will be investigated to provide operating bounds as to what is possible from an experimental design perspective. A higher-fidelity phasic slip model and a thermal-hydraulic mock-up will be required before this sparging design can be implemented.

The effect of bubble removal efficiency on the radioactivity levels, decay heat,

and percentage of Xe extracted into the off-gas system is seen in Table VIII below. The decay heat and radioactivity calculated in the off-gas system, as shown in the Table VIII result purely from the extraction of Xe species and their subsequent daughter species Ce, La, Ba, and Cs.

Table VIII. Impact of bubble removal efficiency on the extraction rate of Xe. The model parameters assume a 2×10^{-6} mol/s He injection rate and an initial bubble diameter of 2 mm.

Bubble Removal Efficiency (%)	Radioactivity in Off-Gas (Ci)	Decay Heat in Off-Gas (W)	Xe Extracted to Off-Gas (%)
8%	1,693.0	51.7	49.9
80%	73.2	2.25	0.04

The two extreme bubble removal efficiency cases illustrate a dramatic difference in the amount of IFPs extractable to the off-gas system. For high bubble-removal efficiency, the bubbles should not circulate throughout the entire loop, but only exist in the riser, with very few being recirculated. This diminishes the overall amount of bubbles and their total residence time in the system, resulting in limited Xe extraction. On the other hand, when bubble removal is diffusion-controlled and there is significant bubble recirculation in the loop, a larger amount of Xe has time to interact with the bubbles, so a larger amount is eventually extracted to the off-gas system.

IV.A.2. Analysis of Te Deposition in the Loop and Off-Gas System

One species of particular interest for tracking is Te. It was noted during the MSRE that Te sometimes acts as a soluble liquid and sometimes as an NM, depending on the redox potential of the fuel salt; in addition, Te causes intergranular corrosion cracking in certain alloys [29]. In this analysis, Te is treated completely as an insoluble

NM. ^{136}Te and ^{133m}Te results are showcased in Table IX (below) to show the effect of short and longer half-lives on the spatial deposition in the loop and off-gas system.

Table IX. Steady-state fraction of insoluble Te spatial distribution highlighting the impact of half-life on deposition in the loop and off-gas system. The model parameters assume a 2×10^{-6} mol/s He injection rate, an initial bubble diameter of 2 mm, and 8% removal efficiency.

	$T_{1/2}$	Liquid	Wall	Gaseous	Off-gas
^{136}Te	17.5 s	86.6%	3.3%	8.5%	1.6%
		2.5×10^{-2} μg/cm^3	1.8 μg	4.6 μg	0.9 μg
^{133m}Te	55.4 m	3.3%	24.2%	1.9%	70.6%
		0.4 μg/cm^3	5.6 mg	0.4 mg	16.4 mg

As seen in Table IX, a short half-life does not provide the ^{136}Te species enough time to plate out on the walls or bubbles or be extracted into the off-gas system, so the majority of the species remains dispersed in the same liquid it was first generated in and in which it rapidly decays while staying in the liquid regime. On the other hand, the longer half-life of ^{133m}Te affords it enough time to interact with walls and bubbles, resulting in the majority of this species being present in the off-gas system or on the walls in VESIL. Bubble removal efficiency will determine whether the majority of long-lived Te is found on the walls of the loop or on the liquid-gas interface at the top of VESIL at the entrance of the off-gas system, since these two sink terms become dominant over the decay period. While the majority of ^{133m}Te species are found predominantly in the off-gas (70%), notable amounts also deposit on the wall (5.6 mg) and remain dissolved in the salt (0.7 mg). The dynamics of these shorter-lived species will have an impact on corrosion in the experiment by affecting the total quantity of Te in the salt and on the walls.

In summary, VESIL is shown to generate appreciable amounts of radionuclides—such as Xe in the off-gas and Te in the salt/wall—to provide invaluable results from an experiment standpoint. Online analysis of the off-gas would provide invaluable data for source-term characterization, while the presence of Te (and other species) will be useful for corrosion evaluations. More detailed time-dependent analyses are required to determine the exact quantities and locations of all IFP species (as well as some separate-effect experimental measurements of the mass transfer coefficients assumed), but this preliminary analysis does highlight the relative utility of the proposed experiment. Through careful design of the helium gas sparging system, the extraction and behavior of IFP species can be controlled and utilized to analyze the ongoing irradiation of fuel salt in the ATR. For example, a realistic gas injection system with only 8% removal efficiency could generate more than 1,000 Ci of Xe in the off-gas system.

V. CONCLUSION

A circulating, fuel-bearing salt irradiation loop would provide invaluable data to the MSR community. This would include corrosion measurement, source term assessment, and monitoring of thermophysical property evolution with burnup. A range of samples and instrumentations can be envisaged to be fitted within the loop to continuously monitor the experiment performance and qualify fueled salt for usage in a reactor. Additionally, post-irradiation examination (PIE) can shed additional insight on the salt composition and its impact on the wall material. These different types of data are expected to be especially invaluable to less tested salts, notably those with chloride solvents.

This research work set out to assess the feasibility of deploying such a capability inside the ATR in order to generate useful conditions for experimental measurements.

Multiple design iterations of the VESIL concept were conducted to reach promising design specifications. It was demonstrated that a relatively compact system with less than 10 kg of fuel salt could induce a temperature difference and natural circulating flow of 60 K and 0.15 m/s, respectively. This is achieved by fine-tuning two axial heat conduction systems: a gas-gap and a fin-gap. The combination of fission product concentration, temperature gradients, and salt velocity is crucial for qualifying the corrosive behavior of MSR systems during operations. Additionally, sensor networks (e.g. thermocouples, flowmeters, needle probes, pressure gauges) can be leveraged to triangulate the evolution of certain thermophysical properties of the salt with time. Further work is needed to qualify these sensors for both the corrosive and irradiation environment.

The experiment generates a maximum power density of 72 W/cm^3 in the I-9 position of the test reactor, and the salt volume-averaged burnup after one cycle would be slightly less than 1 GWd/MTU. The corresponding fission rate would generate appreciable quantities of radionuclides of interest—both for source-term and corrosion studies. Species mass tracking in CTF was conducted to explore design parameters for an off-gas system. A system with 8% removal efficiency would generate over 50 W of Xe-based heat in the off-gas and deposit an appreciable fraction of Te isotopes on the experiment wall (5.6 mg of the short-lived ^{133m}Te). Quantifying the quantity of radionuclides outside the salt will prove invaluable for developing and validating a mechanistic source term model for MSRs. These preliminary evaluations highlight the need for this kind of experimental setup and validate its ability to generate useful data.

ACKNOWLEDGEMENTS

The authors would like to thank Calvin Downey for assistance with generating CAD

drawings and offering guidance on engineering considerations. Joe Palmer and Greg Core also provided valuable feedback on the experiment design and characteristics. The authors would also like to acknowledge the helpful discussions with Dr. Robert Salko Jr. from Oak Ridge National Laboratory (ORNL) on species transport modeling capabilities in the CTF code and his support to allow access to CTF and the ORNL computing facilities

The research work was prepared for the U.S. Department of Energy, through the INL LDRD Program, grant number 20A1049-015FP, under the DOE Idaho Operations Office. It also made use of INL's high-performance computing resources. Contract No. DE-AC07-05ID14517. Lastly, the second author was also supported by a Department of Energy, Office of Nuclear Energy, Integrated University Program Graduate Fellowship.

REFERENCES

[1] J. Kalilainen et al., "Evaporation of materials from the molten salt reactor fuel under elevated temperatures," *Journal of Nuclear Materials*, accepted 23 March 2020.

[2] D. Allen et al., "An investigation of the radiochemical stability of ionic liquids," Green Chem., vol. 4, no. 2, pp. 152–158, 2002.

[3] G. V. Buxton, C. L. Greenstock, W. P. Helman, and A. B. Ross, "Critical Review of rate constants for reactions of hydrated electrons, hydrogen atoms and hydroxyl radicals (·OH/·O−in Aqueous Solution," *J. Phys. Chem. Ref. Data*, vol. 17, no. 2, pp. 513–886, 1988.

[4] H. Hagiwara, S. Sawamura, T. Sumiyoshi, and M. Katayama, "Pulse radiolysis study of transient species in LiCl-KCl melt," *Int. J. Radiat. Appl. Instrumentation. Part C. Radiat. Phys. Chem.*, vol. 30, no. 2, pp. 141–144, Jan. 1987.

[5] J. F. Wishart and P. Neta, “Spectrum and reactivity of the solvated electron in the ionic liquid methyltributylammonium bis(trifluoromethylsulfonyl)imide,” J. *Phys. Chem. B*, vol. 107, no. 30, pp. 7261–7267, Jul. 2003.

[6] W. Phillips et al., “Design and performance of high-temperature furnaces and cell holder for in-situ spectroscopic, electrochemical, and radiolytic investigations of molten salts in extreme environments,” *Rev. Sci. Inst.*, Under Review.

[7] H. E. McCoy, “Status of material development for Molten Salt Reactors,” Oak Ridge National Laboratory, ORNL/TM-5920, January (1978).

[8] K. Sridharan and T. R. Allen, “Chap 12: Corrosion in Molten Salts,” *Molten Salt Chemistry*, pp. 241–67 (2013).

[9] G. F. Flanagan, D. E. Holcomb, and W. P. Poore, “Molten Salt Reactor Fuel Qualification Considerations and Challenges,” Oak Ridge National Laboratory, ORNL/LTR-2018/1045, November 2018.

[10] A. Abou-Jaoude et al., “Evaluation of a Versatile Experimental Salt Irradiation Loop (VESIL) inside the Advanced Test Reactor,” Idaho National Laboratory, INL/EXT-19-52917, May 2019.

[11] National Scientific User Facility, “Advanced Test Reactor National Scientific User Facility Users' Guide,” Idaho National Laboratory, INL/EXT-08-14709, (2009).

[12] D. B. Trauger and J. A. Colin, "Circulating Fused-Salt Fuel Irradiation Test Loop," *Nuclear Science and Engineering*, vol. 9, pp. 346–356, 1961.

[13] H. C. Savage, E. Campere, J. M. Baker and E. G. Bohlmann, "Operation of Molten-Salt Convection Loops in the ORR," Oak Ridge Naitonal Laboratory, 1960.

[14] C. W. Forsberg, P. F. Peterson, K. Sridharan, L. Hu, M. Fratoni and A. Kant-Prinja, "Integrated FHR Technology Development: Trititum Management, Materials

Testing, Salt Chemistry Control, Thermal Hydraulics and Neutronics, Associated Benchmarking and Commercial Basis," NEUP Report, MIT-ANP-TR-180, 2018.

[15] P. R. Hania, "MSR Irradiation Program at NRG Petten," in *MSR Workshop 2018*, Oak Ridge, TN, 2018.

[16] W. H. Jordan, S. J. Cramer and A. J. Miller, "Airecraft Nuclear Propulsion Program: Quarterly Progress Report for Period Ending December 31, 1956," Oak Ridge National Laboratory, ORNL-2221, 1957.

[17] J. J. Powers, N. R. Brown, D. E. Mueller, B. W. Patton, E. Losa and M. Kostal, "Sensitivity/uncertainty analyses comparing LR-0 reactor experiments containing FLiBe salt with models for molten-salt-cooled and molten-salt-fueled reactors," *Annals of Nuclear Energy*, vol. 120, pp. 319–332, 2018.

[18] N. D. Ezell, J. McDuffee, K. Smith and S. Raiman, "Initial Irradiation Testing of Chloride Salts for Molten Salt Reactors," in *ANS Winter Meetin*g, Orlando, 2018.

[19] D. Pelowitz et al., "MCNP6 User's Manual, v1.0," Los Alamos National Laboratory, LA-CP-13-00634, (2013).

[20] A. Mourogov and P. M. Bokov, "Potentialities of the fast spectrum molten salt reactor concept: REBUS-3700," *Energy Conversion and Management*, vol. 47, pp. 2761–2771, 2006.

[21] C. Permann et al., “MOOSE: Enabling Massive Parallel Multiphysics Simulation,” *SoftwareX*, **11**, pp. 100430, (2020).

[22] R. Hu, "A fully-implicit high-order system thermal-hydraulics model for advanced non-LWR safety analyses," *Annals of Nuclear Energy,* **101**, pp. 174–181, (2017).

[23] V. N. Desyatnik, S. F. Katyshev, S. P. Raspopin and Y. F. Chervinskii, "Density, Surface Tension, and Viscosity of Uranium Trichloride-Sodium Chloride Melts," *Atommaya Energiya*, vol. 39, no. 1, pp. 70–72, 1975

[24] M. Altahhan et al., " 3D Coupled Transient simulation of a Fast Liquid Fuel Molten Salt Reactor Primary Loop Using GeN-Foam," in *Proceedings of NURETH-18*, Portland, OR, August 2019.

[25] S. Bhaskar, A. Abou-Jaoude, "Preliminary Design Evaluation of a Natural Circulation Molten Salt Irradiation Loop," in *Transactions of the American Nuclear Society*, Washington D.C., November 2019.

[26] B. Durtschi et al., "Novel Intermediate Conductivity Experiment (NICE) Capsules for Irradiated Fuel," in *Transactions of the American Nuclear Society*, Vol. 120, Minneapolis, Minnesota, June 9–13, 2019.

[27] Z. Taylor, R. Salko, and B. Collins, "Implementation of General Species Transport Capability into VERA-CS for Molten Salt Reactor Analysis," in *Transactions of the American Nuclear Society*, **118**, pp. 1061–1064 (2018).

[28] S. Walker, A. Abou-Jaoude, Z. Taylor, R. Salko, and W. Ji, "Coupled Thermal-Hydraulic Analysis and Species Mass Transport in a Versatile Experimental Salt Irradiation Loop (VESIL) Using CTF," in *Proceedings of PHYSOR 2020*, Cambridge, April 2020.

[29] V. Ignatiev et al. "Intergranular Tellurium Cracking of Nickel-Based Alloys in Molten Li, Be, Th, U/F Salt Mixture," *Journal of Nuclear Materials*, **440**, pp. 243–249, 2013.

[30] S. Walker, Z. Taylor, R. Salko, B. Collins, and W. Ji, "Noble Metal Mass Transport Model for Molten Salt Reactor Analysis in VERA-CS," in *Proceedings of M&C 2019*, Portland, OR, pp. 2268–2277 (2019).

[31] ASME, “BPVC Section III-Rules for Constructions of Nuclear Facility Components-Subsection NCA-General Requirements for Division 1 and Division 2,” ASME BPVC.III.1.ND-2017.

[32] R. J. Kedl, “The Migration of a Class of Fission Products (Noble Metals) in the Molten-Salt Reactor Experiment,” ORNL-TM-3884 (December 1972).